

Topological Features of Both Electron Density and Electrostatic Potential in the Bis(thiosemicarbazide)zinc(II) Dinitrate Complex

Sladjana B. Novaković,[†] Goran A. Bogdanović,^{*,†} Bernard Fraisse,[‡] Nour Eddine Ghermani,^{‡,§} Nouzha Bouhaida,^{||} and Anne Spasojević-de Biré^{*,‡}

Laboratory of Theoretical Physics and Condensed Matter Physics, “VINČA” Institute of Nuclear Sciences, P.O. Box 522, 11001 Belgrade, Serbia, Laboratoire “Structures Propriétés et Modélisation des Solides”, UMR CNRS 8580, Ecole Centrale Paris, Grande Voie des Vignes 92295 Châtenay-Malabry Cedex, France, Laboratoire “Physico-Chimie, Pharmaceutique et Biopharmacie”, UMR CNRS 8612, IFR 141, Faculté de Pharmacie, Université Paris-Sud, 5 Rue Jean-Baptiste Clément, 92296 Châtenay-Malabry Cedex, France, and Laboratoire “Sciences des Matériaux”, LSM, Faculté des Sciences Semlalia, Université Cadi Ayyad, Boulevard Prince Moulay Abdallah, BP 2390, 40000 Marrakech, Morocco

Received: July 12, 2007; In Final Form: September 26, 2007

The experimental electron density of the bis(thiosemicarbazide)zinc(II) dinitrate complex, $[\text{Zn}(\text{CH}_5\text{N}_3\text{S})_2](\text{NO}_3)_2$, was studied. The Hansen–Coppens multipole model was used to extract the electron density from high-resolution X-ray diffraction data collected at 100 K. Careful strategies were designed for the electron density refinements regarding the charge transfer between the anionic and the cationic parts of the complex. Particular attention was also paid to the treatment of the electron density of the zinc atom interacting with two thiosemicarbazide ligands in a tetrahedral coordination. Nevertheless, the filled 3d valence shell of Zn was found unperturbed, and only the 4s shell was engaged in the metal–ligand interaction. Topological properties of both electron density and electrostatic potential, including kinetic and potential energy densities, and atomic charges were reported to quantify a metal–ligand complex with particular Zn–S and Zn–N bonds and hydrogen-bonding features. Chemical activities were screened through the molecular surface on which the three-dimensional electrostatic potential function was projected. The experimental results were compared to those obtained from gas-phase quantum calculations, and a good agreement was reached between these two approaches. Finally, among other electrostatic potential critical points, the values at the maxima corresponding to the nuclear sites were used as indices of the hydrogen-bonding capacity of the thiosemicarbazide ligand.

Introduction

Metal–ligand bonding features represent an interesting area of investigation in transition metal chemistry and also in bioinorganic research. Among transition metals in biology, zinc is the second most abundant metal, following iron. It is essential for the functionalities of a number of metalloproteins, expressing both catalytic and structural roles.^{1–3} In biological systems, the zinc ion forms complexes with proteins and nucleic acids. Zinc is very flexible considering the number of coordinated atoms, which can vary from 4 to 7; however, in the cases of enzymes and zinc finger proteins, the cation is usually tetrahedrally coordinated.¹ Biological zinc is only present as d¹⁰ Zn(II); thus most of the common spectroscopic techniques cannot provide sufficient information about metal–ligand bonding.⁴

Thiosemicarbazide-based compounds have been extensively studied over the last couple of decades.⁵ The various Schiff bases of thiosemicarbazide (the thiosemicarbazones) and their corresponding complexes have attracted much attention due to their

very wide biological activities.⁶ Among them, complexes of Zn with different thiosemicarbazones show evident antitumor activities.⁶ In one of the most recent studies, Cowley et al. have demonstrated that Zn bis(thiosemicarbazone) complexes reveal a use for their intrinsic fluorescence for the illumination of cancer cells,⁷ while Kovala-Demertzi et al. have shown that some complexes of zinc with thiosemicarbazone derivatives are similar or better than *cis*-platin drug in their anti-proliferative activities *in vitro*.⁸

The thiosemicarbazide (TSC) itself, $\text{N}^1\text{H}_2\text{—N}^2\text{H—C(=S)—N}^3\text{H}_2$, and its metal complexes do not show any biological activities. However, recent investigations in the field of supramolecular chemistry find some of these complexes suitable building blocks or so-called “synthons” for supramolecular structures.^{9,10} Owing to the fact that the thiosemicarbazide is a relatively small unit, it possesses considerable hydrogen donor capacity and therefore can be easily incorporated into hydrogen-bonding systems. Using the $[\text{M}(\text{TSC})_2]^{2+}$ complex cations ($\text{M} = \text{Ni}$ and Zn) and the anions of different dicarboxylic acids, Burrows et al.⁹ have developed a synthetic method for generation of supramolecular arrays with the incorporated metal ions.^{9,10} In the aggregation process for these ionic species, particular importance has been devoted to the complementary hydrogen bonding formed between the pair of donors (N^2 , N^3) of the thiosemicarbazide complex and the pair of acceptors that are the oxygen atoms of the carboxylate group. The complementary

* Authors to whom correspondence should be addressed. Phone: +381-11-8065-828 (G.A.B.); 33-1-41-13-15-90 (A.S.). Fax: +381-11-8065-829 (G.A.B.); 33-1-41-13-14-37 (A.S.). E-mail: goranb@vin.bg.ac.yu; anne.spasojevic@ecp.fr.

[†] “VINČA” Institute of Nuclear Sciences.

[‡] Ecole Centrale Paris.

[§] Université Paris-Sud.

^{||} Université Cadi Ayyad.

hydrogen bonding, which is assigned in Etter's graph set notation¹¹ as a $R(8)_2^2$ motif, has been considered as the basis of the process of self-assembly.

In the synthesis of all $[\text{Zn}(\text{TSC})]^{2+}$ polymers such as $[\text{Zn}(\text{TSC})_2(\text{H}_2\text{O})_2](\text{tere})\cdot\text{H}_2\text{O}$,^{9b} $[\text{Zn}(\text{TSC})_2(\text{H}_2\text{O})_2](\text{fum})$,^{9d} $[\text{Zn}(\text{TSC})_2(\text{citr})\cdot\text{H}_2\text{O}$,^{9d} and $\{[\text{Zn}(\text{TSC})(\mu-\kappa^1, \kappa^2 1, 2\text{-malonate})]\cdot\text{H}_2\text{O}\}_n$,^{9a} (tere = terephthalate, fum = fumarate, and citr = citraconate), TSC has been used to provide the cationic synthon for these aggregates. Moreover, besides the donor capacity of TSC in building up hydrogen-bonded polymers, the formed M–L bonds are sufficiently strong due to the high coordination abilities of the TSC ligand. Consequently, this ligand will be not replaced with, for example, the terephthalate anion, known as a rather strong ligand¹² and which in this case would only serve as a hydrogen bond acceptor (anionic synthon).

Among the different methods employed to investigate the nature of the chemical bonds and noncovalent interactions, experimental charge density analysis^{13a} has proven to be very useful because it offers information on the electronic level.¹³ Due to the particular electronic configuration of the zinc atom ($3d^{10}4s^2$) with a filled 3d shell unaffected by the ligand field strength¹⁴ and energetically stable with respect to the acceptor ligand, this element is particularly interesting from the aspect of the charge density analysis. However, in the case of the zinc-containing compounds (including coordination and inorganic complexes), very few publications have been reported.^{15–17} To our knowledge, only two of them describe the electronic properties of the zinc complex compounds.^{16,17}

The octahedral $[\text{Zn}(\text{C}_4\text{O}_4)(\text{H}_2\text{O})_4]$ has been investigated as a part of the systematic charge density study performed to explore the bonding properties of different 3d metal ions to the squarate ligand.¹⁶ These complexes showed consistent deformation density and topological features; however, in contrast to Fe, Co, and Ni ions, which are nearly neutral, Zn was found to be highly positively charged (+1.97 e). The total number of d electrons was also refined and was found to be equal to 8.4 e for Zn. In the experimental charge density of the tetrahedral $[\text{Zn}(\text{aspirinate})_2(\text{H}_2\text{O})_2]$, $3d^{10}$ metal bonding to a drug ligand has been investigated. The analysis revealed that in this complex only the Zn 4s orbital participates in the interaction with the ligand, while the metal 3d shell remains unperturbed. In this compound, the net atomic charge of Zn was found to be equal to +1.29 e.¹⁷

In the present study, we present the results for the experimental charge density of the $[\text{Zn}(\text{TSC})_2](\text{NO}_3)_2$ complex where the zinc metal is tetrahedrally coordinated to the simple bidentate ligand, thiosemicarbazide, $\text{N}^1\text{H}_2\text{—N}^2\text{H—C(=S)—N}^3\text{H}_2$, comprising N and S donor atoms. The crystal structure of $[\text{Zn}(\text{TSC})_2](\text{NO}_3)_2$ has been derived at room temperature by Romanenko et al.^{18a} and Tong et al.^{18b} Considering the quality of the crystallographic data in both cases, this structure could be classified as one of the best among the thiosemicarbazide-based structures deposited in the Cambridge Structural Database (CSD).¹⁹ Such a property makes it very suitable for an experimental charge density analysis.

High-resolution and accurate experiments at low temperature (100 K) have been performed. This allows careful analysis of the electron density distribution in the $[\text{Zn}(\text{TSC})_2](\text{NO}_3)_2$ complex. Through these analyses, we have gained additional insight into the nature of the M–L bond for a metal filled d orbital. As far as we know, this is the first charge density study of any transition metal complex with a thiosemicarbazide-based ligand. However, the electron densities of two TSC-based

ligands have already been studied: 1-formyl-3-thiosemicarbazone²⁰ and salicylaldehyde thiosemicarbazone.²¹

We also explore the coordination properties of the nonsubstituted ligand at the electronic level by ab initio calculations. Bear in mind that the N^1S coordination mode and the formation of five-membered chelate ring represent the basic properties of almost all TSC-based transition metal complexes.⁵ Due to the presence of the nitrate group as an anion, the title compound also forms an extensive hydrogen-bonding network. It contains the above-described complementary $R(8)_2^2$ hydrogen-bonding motif,¹¹ which is, in this case, formed with the nitrate oxygen as the acceptor pair. Thus, we were prompted to explore the complex system of the hydrogen-bonding interactions present in this crystal structure. Subsequent application of the topological analysis²² to the determined experimental electron density was of particular significance in revealing the nature of the chemical bonds and interactions. Finally, because the title compound is used as a reactant in supramolecular synthesis, we have derived the net atomic charges and electrostatic potential within this molecule in an attempt to understand its further reactivity.¹³

Experimental Section

Data Collection. A well-formed colorless crystal sample of $[\text{Zn}(\text{TSC})_2](\text{NO}_3)_2$, with dimensions $0.47 \times 0.43 \times 0.30$ mm³, was chosen for the high-resolution X-ray diffraction experiment. The data were collected at 100.0(1) K on a Bruker-SMART three-axis diffractometer equipped with a SMART 1000 charge coupled device (CCD) area detector using graphite monochromated Mo $K\alpha$ X-ray radiation (wavelength $\lambda = 0.71073$ Å). The low temperature was reached by an evaporated liquid nitrogen flux over the crystal, provided by the Oxford Cryo-system device. The area detector surface was placed at 4.08 cm from the crystal sample. The diffraction data were collected at five different detector positions, $2\theta = 0^\circ, 28^\circ, -45^\circ, 60^\circ$, and -85° , where θ is the Bragg angle. The diffraction data were collected as ω -scans with a scan width of -0.15° . The maximum resolution reached for this experimental data set was $(\sin \theta/\lambda)_{\text{max}} = 1.10$ Å⁻¹. The Lorentz polarization correction and the integration of the diffracted intensities were performed with the SAINT software package.²³ The final refined cell parameters are given in Table 1. An empirical absorption correction was applied using the SADABS computer program.²³ The SORTAV program²⁴ has been used for final data sorting and averaging of 55 584 reflections collected, giving a total of 7616 unique reflections with final $R_{\text{int}} = 1.7\%$. In the conventional and multipole refinement, a total of 5904 reflections were used. The deposition number of the crystallographic data is CCDC 653751.

Electron Density Distribution. The Hansen–Coppens multipole model has been used for the description of the molecular electron density²⁵

$$\rho_{\text{at}}(r) = \rho_{\text{core}}(r) + P_{\text{val}}\kappa^3\rho_{\text{val}}(\kappa r) + \kappa'^3 \sum_{l=0}^{l_{\text{max}}} R_{nl}(\kappa' r) \sum_{m=0}^l P_{lm} \pm y_{lm} \pm(\theta, \varphi) \quad (1)$$

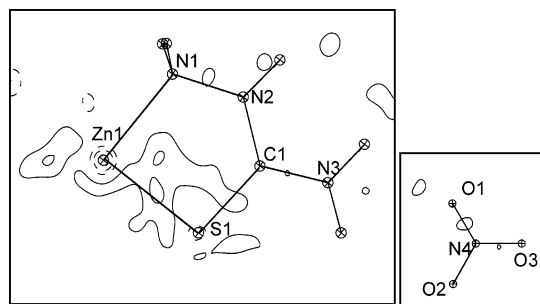
According to this model, the electron density of each atom is given as a sum of a core electron density (ρ_{core}), a spherical valence electron density (ρ_{val}), and a spherical part of the atomic electron density. The core and valence electron densities are both obtained from the Hartree–Fock wave function of the free atoms or ions. κ is a contraction–expansion coefficient that modifies the radial distribution of the valence electron density. It is refined along with the P_{val} parameter that represents valence

TABLE 1: Crystallographic Details

empirical formula	[Zn(CH ₃ N ₃ S) ₂](NO ₃) ₂
formula weight (g mol ⁻¹)	371.7
crystal system	monoclinic
space group	C2/c
crystal size, color	0.47 × 0.43 × 0.30, colorless
<i>a</i> (Å)	10.9541(3)
<i>b</i> (Å)	7.5673(2)
<i>c</i> (Å)	14.1753(3)
α (deg)	90
β (deg)	101.630(2)
γ (deg)	90
<i>Z</i>	4
volume (Å ³)	1150.90(6)
density (g cm ⁻³)	2.15
μ (mm ⁻¹)	2.54
<i>T</i> (K)	100.0(1)
λ (Å)	0.71073
($\sin \theta/\lambda$) _{max} (Å ⁻¹)	1.10
no. of data collected	55 584
no. of unique reflections	7616
<i>R</i> _{int} (%)	1.67
Conventional Refinement by SHELX	
no. of reflections used	6178
<i>R</i> (%)	1.90
<i>R</i> _w (%)	4.40
goodness of fit	1.03
Multipole Refinement	
no. of reflections used (<i>I</i> > 3 σ (<i>I</i>))	5904
<i>R</i> [<i>F</i>] (%)	1.15
<i>R</i> _w [<i>F</i>] (%)	1.33
goodness of fit	0.88

electron population. The atomic charge thus can be estimated as $q = P_{\text{val}} - N_{\text{val}}$, where N_{val} is the population of the free atom. The final term that describes the aspherical part of the electron density is given as a series of density-normalized spherical harmonics. The radial part for the deformation function is given as Slater type function $R_{nl}(r) = Nr_l^n \exp(-\xi_l r)$, where N is a normalization factor. In eq 1, κ' is the contraction-expansion coefficient of the radial part of aspherical valence shell, while P_{lm} are multipole population parameters. The ξ_l exponents (in bohr⁻¹) are chosen to be equal to 3.0 and 4.5, and $n_l = 2, 2,$ and 3 up to octupoles ($l = 3$) for C and O atoms respectively; $\xi_l = 2.26$ bohr⁻¹ and $n_l = 1$ (dipole level, $l = 1$) for the hydrogen atoms; $\xi_l = 4.1$ bohr⁻¹ and $n_l = 4, 4, 4,$ and 6 up to hexadecapole ($l = 4$) for S. Taking into account the special position of the metal ion, the local coordinate system for the Zn atom was defined in such a way that the principal axis was parallel to the 2-fold axis. (The local axis divides the interligand angle S1–Zn–S1'; i.e., it is directed toward the dummy atom placed in the middle point of the S1...S1' line.) For all refinements in this study, the P_{val} population was always assigned to the diffuse 4s electron density of the zinc metal atom.

Refinement Strategies. The crystal structure was determined on the basis of accurate low-temperature data using the WinGX program packing.²⁶ Conventional and electron density refinements were performed with the MOLLY program implementing the Hansen–Coppens multipole model.²⁵ In the first cycles of the refinements, to obtain the best estimation of the atomic positional and thermal parameters for non-hydrogen atoms, the high-order ($\sin \theta/\lambda > 0.8$ Å⁻¹) refinement strategy was first applied. Residual Fourier maps calculated with high-order data revealed features of the anharmonic thermal motion for Zn; thus Gramm–Charlier expansion²⁷ up to the sixth order was included for Zn during the refinement. Before the electron density refinement, the positions of hydrogen atoms were extended to

**Figure 1.** Residual electron density maps: (a) Zn1–C1–N1 plane; (b) N4–O3–O1 plane. The contour interval is 0.1 e Å⁻³, negative contours are dashed, and zero contour is omitted.**TABLE 2: Labeling of the Compounds Used in This Paper**

compound	reference	CSD code
NH ₂ –NH–C(=S)NH ₂ TSC	30	TSCRBZ20
[Zn(TSC) ₂ (H ₂ O) ₂](tere)	9g	PABQEO
[Zn(TSC) ₂ (H ₂ O) ₂](fum)	9d	RUZPIL
[Zn(TSC) ₂ (citr)]·H ₂ O	9d	RUZPOR
[{[Zn(TSC)(μ - κ^1, κ^2 1,2-malonate)]·H ₂ O} _n	9a	QARTOT
[Zn(C ₄ O ₄)(H ₂ O) ₄]	16	
[Zn(aspirinate) ₂ (H ₂ O) ₂]	17	
[Zn(TSC) ₂](NO ₃) ₂	18a,b, this work	DASFUY
NH ₂ –NH–C(=S)NH ₂ TSCH ⁺	31	TSEMHC

the corresponding neutron distances.²⁸ The N–H bond lengths are relaxed in the last cycle of the refinement.

Two strategies have been applied during the multipole refinement. In the first case, the neutrality constraint was imposed on the complex as a whole, allowing for charge transfer between the ionic species (strategy **I**). This refinement started by considering a neutral zinc atom with separated 3d and 4s valence shells. In the second refinement, the charges within the ions are constrained to +2 for the cation and –1 for each anion, not allowing a charge transfer between the ions (strategy **II**). At the beginning of the refinement by strategy **II**, the positive charge of +2 was located on Zn ($P_{\text{val}} = 0$), while the excess of negative charge of 1 e was split between the oxygen atoms of the NO₃ anion. All attempts to refine the Zn multipole parameters failed and have yielded unrealistic 3d occupations larger than 2 electrons per orbital. However, with fixed $P_{00}(3d)$ it was possible to refine Zn multipole parameters, and these results are presented in the second part of the Supporting Information. Consequently, in the final strategies (**I** and **II**), the second monopole $P_{00}(3d)$ value was fixed at 10 e, whereas multipole parameters were set to zero; that is, only the Zn 4s orbital interaction with the ligands has been finally considered in this study. A similar refinement method was successfully applied in the case of tetrahedral [Zn(aspirinate)₂(H₂O)₂].¹⁷

The main differences between the results obtained by these two strategies consist of the values of the atomic charges that are calculated after a κ -refinement. Namely, in contrast to strategy **II** where the charges of ions are fixed ($[\text{Zn}(\text{TSC})_2]^{+2}$ and $2(\text{NO}_3)^{-}$), unconstrained strategy **I** led to the values of +1.92(28) and –0.95(10) e for the cation and each of the anions, respectively. The statistical least-square features did not differ significantly between these two strategies; thus the results presented in this work correspond to those obtained by strategy **I**. The detailed results for both strategies are included in the Supporting Information. The crystallographic details are presented in Table 1. Figure 1 represents the residual density map obtained after the multipole refinement for the plane of the complex cation and the NO₃ anion. The residual electron densities are computed as Fourier transformations of the ($F_o -$

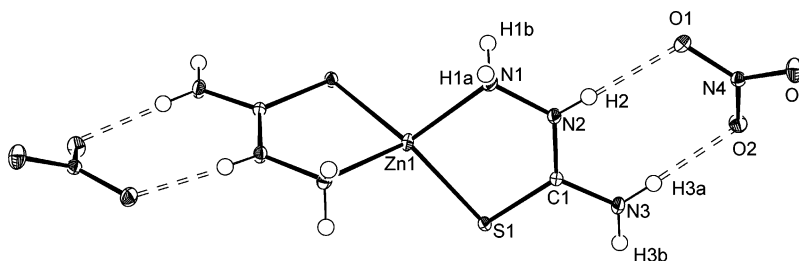


Figure 2. Crystal structure of $[\text{Zn}(\text{TSC})_2](\text{NO}_3)_2$.

TABLE 3: Interatomic Distances and Topological Properties of the Electron Density for the Covalent Bonds^a

bond	length	d_1	d_2	$\rho(r_{\text{cp}})$	$\nabla^2\rho(r_{\text{cp}})$	λ_1	λ_2	λ_3	ϵ	$G(r_{\text{cp}})$	$V(r_{\text{cp}})$	$H(r_{\text{cp}})$
Zn1–N1	2.0918(2)	0.999	1.093	0.52	7.16	–2.89	–2.70	12.76	0.07	234.80	–274.91	–40.11
Zn1–S1	2.2667(2)	1.047	1.221	0.41	5.20	–1.81	–1.68	8.55	0.08	162.44	–187.22	–24.78
N1–N2	1.4114(2)	0.716	0.696	2.06	–3.56	–16.17	–15.10	27.71	0.06	1059.91	–2207.65	–1147.74
C1–N2	1.3419(3)	0.554	0.788	2.35	–22.32	–19.26	–16.72	13.66	0.15	883.40	–2373.71	–1490.31
C1–N3	1.3274(3)	0.554	0.773	2.43	–23.20	–20.58	–16.58	13.95	0.21	941.66	–2514.18	–1572.5
C1–S1	1.7194(2)	0.911	0.809	1.30	–2.61	–7.00	–5.66	10.04	0.24	436.25	–934.47	–507.22
O1–N4	1.2561(2)	0.624	0.632	3.07	–5.83	–26.43	–23.47	44.08	0.13	1919.45	–3997.43	–2077.98
O2–N4	1.2568(3)	0.622	0.635	3.08	–6.03	–26.65	–23.62	44.24	0.13	1926.85	–4017.65	–2090.80
O3–N4	1.2418(3)	0.622	0.619	3.20	–10.82	–28.30	–24.11	41.58	0.17	1973.74	–4241.99	–2268.25
N1–H1a	0.997(10)	0.728	0.296	2.16	–19.49	–28.59	–26.34	33.44	0.09	773.84	–2077.56	–1303.72
N1–H1b	1.030(9)	0.735	0.295	2.06	–16.70	–24.99	–23.12	31.43	0.08	738.79	–1931.69	–1192.90
N2–H2	0.991(10)	0.740	0.250	2.12	–21.76	–29.04	–26.62	33.91	0.09	698.12	–1986.92	–1288.80
N3–H3a	1.006(10)	0.756	0.250	2.14	–27.40	–29.18	–27.31	29.90	0.07	613.10	–1971.24	–1358.14
N3–H3b	0.984(10)	0.722	0.262	2.27	–24.96	–31.35	–29.07	35.46	0.08	771.98	–2222.65	–1450.67

^a d_1 and d_2 are the distances (in Å) from the critical points to atoms 1 and 2, respectively; $\rho(r_{\text{cp}})$ is the electron density (in $\text{e} \text{Å}^{-3}$); $\nabla^2\rho(r_{\text{cp}})$ is the Laplacian (in $\text{e} \text{Å}^{-5}$); λ_1 , λ_2 , and λ_3 are the principle curvatures (in $\text{e} \text{Å}^{-5}$); ϵ is the ellipticity; G , V , and H are kinetic energy density, potential energy density, and total energy density, respectively (in kJ mol bohr^{-3}).

F_c) difference where F_o and F_c were observed and model calculated structure factors. The residual density maps are essentially featureless. The highest residual density peaks of $0.2 \text{ e} \text{Å}^{-3}$ are found in the vicinity of the Zn atom.

Computational Methods. Theoretical calculations have been performed with density functional theory (DFT) calculation methods using the Gaussian 03 program package.²⁹ In the case of the title compound $[\text{Zn}(\text{TSC})_2](\text{NO}_3)_2$ and its TSC ligand (which in the complex displays a cis configuration), the coordinates used in the calculations are those obtained from the multipole refinement. The coordinates of the analyzed Zn supramolecular complexes^{9g,9d} have been extracted from the CSD (Table 2). The coordinates of the two additional forms of the TSC ligand, the *trans*-TSC³⁰ and the protonated *cis*-TSC,³¹ have also been extracted from the CSD. For all extracted compounds, the corresponding N–H bond lengths are elongated to the experimental values obtained after the multipole refinement of the title compound. The optimizations of the molecules were not performed. The calculations of the electrostatic potential and electrostatic potential at the nuclear sites have been performed in a vacuum using the B3LYP functional with the 6-31++G(2d,2p) basis set as suggested by Dudev and Lim for Zn-containing compounds.³

Results and Discussion

Crystal Structure. The crystal structure of the title compound consists of $[\text{Zn}(\text{TSC})_2]^{+2}$ complex cations and nitrate anions. The Zn atom is located in a tetrahedral environment formed by two bidentate thiosemicarbazide ligands comprising N and S donor atoms. Figure 2 depicts the ORTEP view of the crystal structure. Inspection of the geometrical parameters does not reveal a significant difference from the room-temperature data.¹⁸ Due to the small bite angle of the TSC ligand ($88.47(6)^\circ$), the tetrahedral coordination geometry (109.28°) of the complex is significantly deformed. The intermediary values of two N–C

and C=S bond lengths (column 2 in Table 3) suggest a considerable degree of delocalization within the ligand. Consequently, the chelate ring is practically planar with a mean plane deviation of the constituting atoms of 0.014 Å .

Due to the high hydrogen donating capacity of the complex cation and the presence of the NO_3 anion as an acceptor, crystal packing of $[\text{Zn}(\text{TSC})_2](\text{NO}_3)_2$ exhibits a rather complex hydrogen-bonding network. There are nine hydrogen bonds of the same N–H \cdots O type involved in stabilization of the complex. It is important to mention that two of the five hydrogen atoms existing in this structure are involved in a bifurcated and one in a trifurcated hydrogen bond, additionally increasing the complexity of the pattern (Table 4).

As previously mentioned, the complex cation provides a combination of the hydrogen-bonding donors suitably oriented for the interaction with the anion hydrogen-bonding acceptor pair. Thus, complementary hydrogen bonds are formed on each side of the molecule involving hydrazine (N2–H2) and thioamide (N3–H3a) fragments on the ligand side and the O1, O2 acceptor pair of the NO_3 anion. The hydrogen-bonding motif formed in this way (Figure 2) can be assigned in Etter's graph set notation as $R(8)_2$.¹¹ According to geometrical parameters presented in Table 4, these complementary hydrogen bonds exhibit the shortest lengths and very good directionality (with quite large N–H \cdots O angles). In these interactions, donor and acceptor atoms are forming a torsion angle, N2–N3–O1–O2, of 8.2° . However, the dihedral angle formed between the mean planes of the chelate ring and the nitrate anion is 31.1° . It seems that the engagement of the third oxygen atom of the NO_3 anion in the additional relatively strong N1–H1a \cdots O3 hydrogen bond slightly shifts the acceptor plane. This third hydrogen bond connects the neutral complex molecules into an extended ribbon as presented in Figure 3a. Due to the presence of the second row axis passing through the metal ion and changing the orientation of the donors, the ribbon takes a more twisted form.

TABLE 4: Interatomic Distances and Topological Properties of the Electron Density for the Hydrogen Bonds

bond	N \cdots O (Å)	H \cdots O (Å)	N–H \cdots O (deg)	d_1	d_2	$\rho(r_{cp})$	$\nabla^2\rho(r_{cp})$	λ_1	λ_2	λ_3	ϵ	$G(r_{cp})$	$V(r_{cp})$	$H(r_{cp})$
N3–H3a \cdots O2 ⁱ	2.8502(4)	1.8456(3)	175.51(2)	0.622	1.228	0.10	4.07	–0.55	–0.52	5.14	0.08	80.50	–50.33	30.17
N2–H2 \cdots O1 ⁱ	2.9141(3)	1.9239(3)	178.46(3)	0.695	1.229	0.13	2.97	–0.69	–0.68	4.32	0.03	64.25	–47.77	16.48
N1–H1a \cdots O3 ⁱⁱ	2.9272(4)	1.9906(3)	155.56(2)	0.723	1.286	0.08	2.63	–0.47	–0.39	3.47	0.19	52.77	–34.84	17.93
N3–H3b \cdots O1 ⁱⁱⁱ	3.0080(4)	1.9954(2)	156.12(2)	0.800	1.371	0.05	1.82	–0.26	–0.20	2.28	0.25	35.10	–20.71	14.39
N1–H1b \cdots O3 ^{iv}	3.2770(5)	2.2942(4)	159.18(2)	0.907	1.479	0.04	1.13	–0.12	–0.05	1.31	0.87	21.21	–11.97	9.24
N1–H1b \cdots O2 ^{iv}	3.0294(4)	2.4650(3)	108.32(2)	1.078	1.433	0.05	0.94	–0.09	–0.15	1.40	0.57	20.06	–13.21	6.85
N1–H1a \cdots O1 ⁱⁱ	3.4414(4)	2.5542(3)	148.17(1)	1.048	1.621	0.02	0.59	–0.06	–0.03	0.68	0.51	11.16	–6.28	4.88
N3–H3a \cdots O3 ^v	3.0272(4)	2.5737(3)	107.18(2)	1.161	1.471	0.04	0.80	–0.14	–0.13	1.08	0.11	15.96	–10.16	5.80
N1–H1b \cdots O2 ^{vi}	3.0933(4)	2.6111(3)	108.32(1)	1.211	1.501	0.04	0.70	–0.13	–0.07	0.91	0.71	14.15	–9.27	4.88

^a Properties and units are defined in the footnote to Table 3. Symmetry codes: (i) x, y, z ; (ii) $-x + 0.5, -y - 0.5, -z + 1$; (iii) $x + 0.5, y + 0.5, z$; (iv) $x, y, z + 0.5$; (v) $-x + 0.5, y + 0.5, -z + 0.5$; (vi) $-x + 0.5, y - 0.5, -z + 1$.

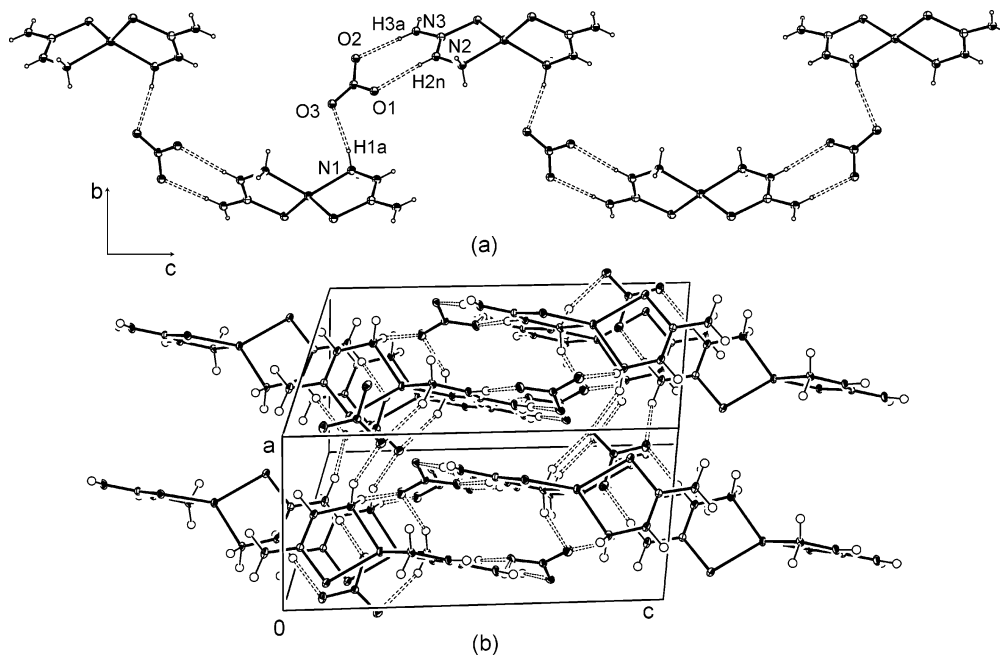


Figure 3. (a) One-dimensional chain formed by the strongest hydrogen bonds. (b) segment of the crystal packing of [Zn(TSC)₂](NO₃)₂.

The ribbons are further mutually interconnected by two medium, N3–H3b \cdots O1 and N1–H1b \cdots O3, and four weaker hydrogen bonds (minor components³²), giving rise to more complex hydrogen-bonded arrangements. Part of the crystal packing is shown in Figure 3b.

Electron Deformation Density and Topological Properties in the Complex Entity. The static electron deformation density maps³³ for the plane of the chelate ring of the complex cation and the nitrate anion are given in Figure 4. Within the planar thiosemicarbazide ligand, the two C–N bonds exhibit the highest bonding densities of similar values, 0.60 and 0.65 e Å^{–3}. The highest density peak is found in the terminal C1–N3 bond, which is in accordance with its shorter length. The densities are well-centered on the bonds and do not show significant polarization. The electron deformation density in the N1–N2 bond of 0.25 e Å^{–3} has the lowest value found in the molecule, while the C=S bond, as a part of the conjugated system, exhibits a much higher electron density peak (0.45 e Å^{–3}).

For a more quantitative characterization of the bonds, a topological analysis of the total electron density has been carried out.^{22,34} The obtained results are listed in Table 3. According to topological features, the differences between the two C–N bonds are more pronounced. The value of the electron density at the bond critical point (BCP) for the terminal C1–N3 bond is higher compared to the C1–N2 bond. The higher value of the ellipticity ϵ and the resulting local total energy densities³⁵

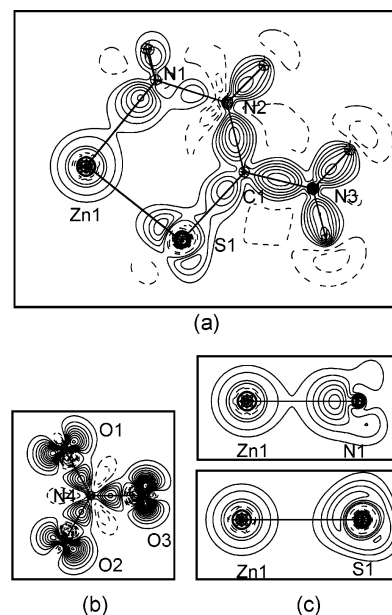


Figure 4. Static electron deformation density maps: (a) Zn1–C1–N1 plane; (b) N4–O3–O1 plane; (c) in the plane orthogonal to the chelate ring. Contours are as in Figure 1.

for the C1–N3 bond indicate slightly higher covalent character for this bond, which is not included in the chelate ring. The

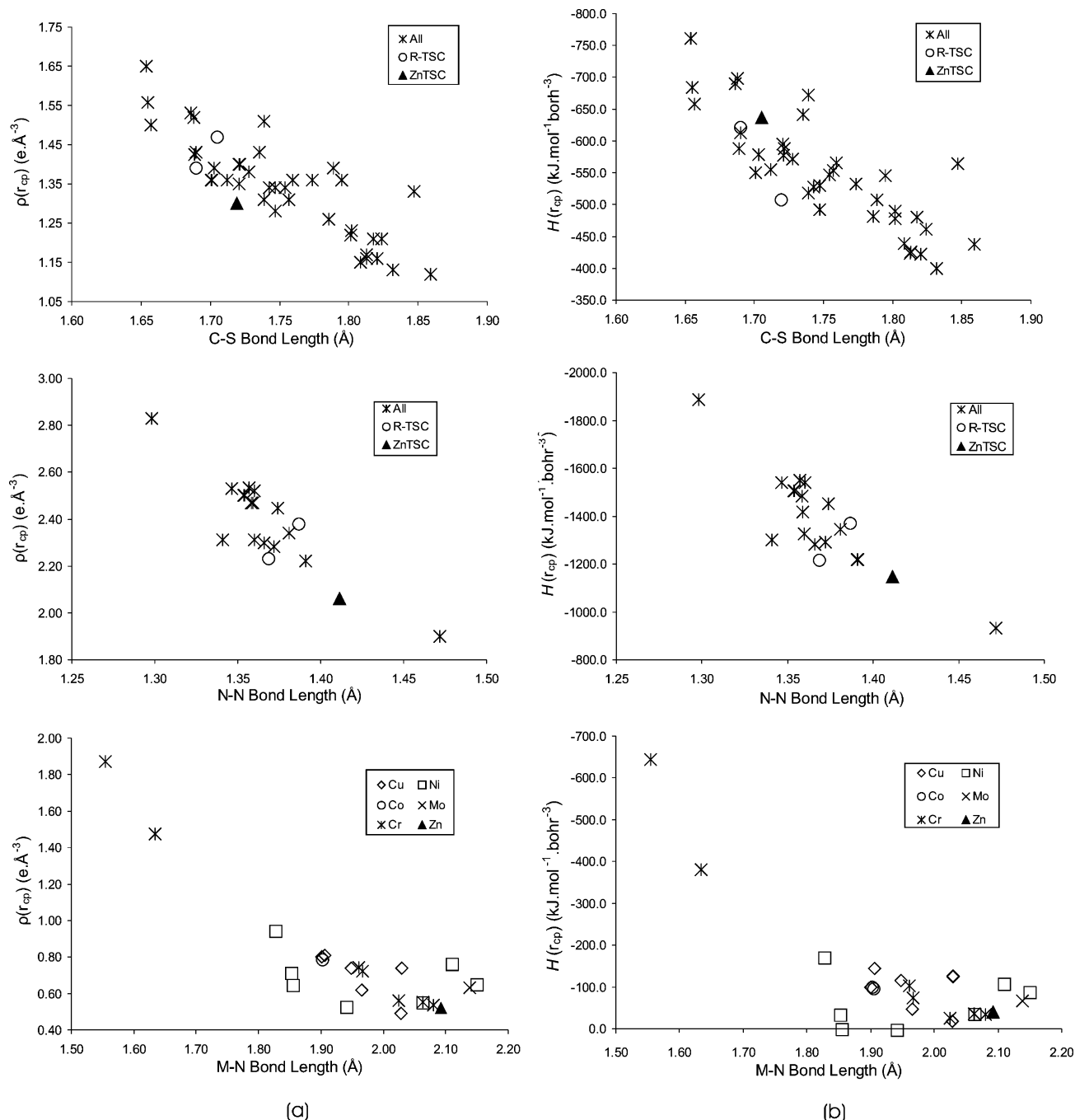


Figure 5. (a) $\rho(r_c)$ vs bond length and (b) $H(r_c)$ vs bond length for C–S, N–N, and M–N bonds.^{36–38} (R–TSC is for other TSC-based compounds.^{20,21})

position of the BCP clearly indicates that both C–N bonds are polarized, and in both cases, the BCP is found at equal distances from the C atoms (0.554 Å). In a recently reported charge density analysis of the uncoordinated TSC derivative 1-formyl-3-thiosemicarbazide,²⁰ very similar topological properties have been reported for the two corresponding C–N bonds. The values of ρ found in the BCP of this ligand are 2.31 and 2.44 $\text{e} \text{Å}^{-3}$, which are almost identical to those found in the present complex.

The values of ρ and the Laplacian at the BCP of the C=S bond are as expected much less than those of the C=N bonds. However, the ellipticity value indicates a significant double bond character, which confirms that the C=S bond is involved in the conjugation process. This is in agreement with the reported C=S bond lengths, which are of intermediary values. The lower value of ellipticity for the N1–N2 bond indicates that this bond is more cylindrical and closer in nature to the single one. The

reported topological features emphasize the conjugation effect, which is particularly present in the thioureide fragment of the ligand. Figure 5 contains the behaviors of the topological parameters ρ and H , obtained from the experiment, as a function of the interatomic distances for the unusual bonds (C–S, N–N, and M–N, where M is a transition metal) of the studied compound. The general trend for the C–S bond^{20,21,36} is a significant decrease of ρ with d values and a relatively lower increase of the H values. The values for the N–N bonds³⁷ are closer due to the smaller range of the $d_{\text{N–N}}$ values.

According to the electron deformation density maps in the plane of the chelate ring (Figure 4a), both N and S donor atoms exhibit electron density directed toward the Zn atom. The deformation density of the nitrogen atom is spared along the Zn1–N1 bond, while in the case of sulfur the lone pair is clearly pointed toward the metal center the corresponding bonding

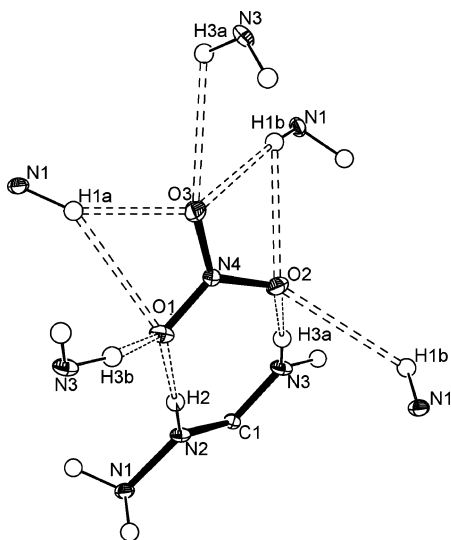


Figure 6. Space distribution of the donor atoms around the nitrate acceptor.

densities are 0.60 and 0.40 $e \text{ \AA}^{-3}$, respectively. Figure 4c presents the electron deformation density of the same bonds in planes perpendicular to the chelate ring. In both cases, the density is concentrated in the plane of the ligand (it is not split above and below the bond), demonstrating the σ donor character of the ligand. Analysis of the Zn1–S1 coordination bond shows that the torus-shaped free electron density of the sulfur donor is described as polarized rather than clearly directed toward the metal ion.

In the topological analysis, the Zn–L bonds are both characterized by positive values of the Laplacian, which is typical for coordination bonds to transition metals. As expected, the Zn–N interaction possesses a larger value of ρ at the BCP. The bond paths of the coordination bonds fall almost exactly on the internuclear axis. The relatively low ellipticities found for these bonds are in accordance with their σ character. The behavior of ρ for the M–N reported values (Figure 5) is in agreement with the interatomic distances, despite the fact that different bond types are compared in the same graph. The relatively very low H values give an indication of the weak strength of these bonds. In coordination bonds, the magnitude of the potential energy density slightly overcomes the value of the kinetic energy density³⁵ ($|V|/G$ is equal to 1.15 for Zn–S and 1.17 for Zn–N), suggesting that these bonds are best described as polar covalent, leading to one of the smallest ratios when compared with the literature for M–N bonds (3 values are in the range of 0.92–0.98, while 20 values are in the range of 1.07–1.7).^{37c,38} The same trend is observed for the M–S bond, but only two experiments have been reported concerning a Ni and a Co complex.^{36e}

Electron Deformation Density and Topology of Hydrogen Bonds. The space distribution of all the hydrogen donor groups around a nitrate acceptor is illustrated in Figure 6. Figure 7a displays the static electron deformation density maps (in N–H...O planes) corresponding to the first three strongest hydrogen bonds, while Figure 7b displays the polarization of each oxygen's lone pair in a plane containing the oxygen atom and the two hydrogen atoms that form the strongest hydrogen bonds. When the oxygen lone pair is involved in the slightly equivalent hydrogen bonds (case of O1), the electron density of the free electron pairs is equitably oriented toward the two hydrogen atoms. This is not the case when one of the hydrogen bonds is significantly stronger than the other one (cases of O2 and O3).

The topological analysis gives a reliable quantitative description of the hydrogen bonds. The BCPs have been found for each of the nine interactions, and the corresponding parameters are given in Table 4. The first two BCPs (first two lines of Table 4) correspond to the shortest and the strongest complementary hydrogen bonds. Although slightly stronger according to its geometrical parameters, the N3–H3a...O2 hydrogen bond shows a lower value of the electron density compared to the other bond from the complementary pair (N2–H2...O1). However, due to the higher value of the Laplacian, the resulting kinetic energy density for the N3–H3a...O2 interaction prevails in magnitude. It should be noted that N3–H3a...O2 is a bifurcated hydrogen bond because the H3a is also engaged in the weakest hydrogen bond to O3. On the contrary, the N2–H2 fragment is involved in an interaction with the single O1 donor (Figure 7).

It is worth pointing out some marked similarities concerning the topology of these bonds. Analyzing the acceptor site, we can find rather equivalent topological parameters for N–O bonds whose oxygen atoms are involved in complementary hydrogen bonding. The N4–O1 and N4–O2 bonds have relatively similar lengths (1.2561(2) and 1.2568(3) \AA , respectively), which are evidently longer than that of the N4–O3 bond (1.2418(3) \AA). The corresponding values of the electron density are similar ($\rho = 3.07$ and 3.08 $e \text{ \AA}^{-3}$ for the N4–O1 and N4–O2 bonds, respectively) and lower than in the case of the third bond ($\rho = 3.20 e \text{ \AA}^{-3}$ for N4–O3), while the values of the Laplacian's (-5.83 and $-6.03 e \text{ \AA}^{-5}$) are nearly half of that found for the third bond ($-10.82 e \text{ \AA}^{-5}$). The ellipticities for N4–O1 and N4–O2 are identical (0.13) and again quite smaller than that in the case of the third bond (0.17). Considering the donors' sites, the N–H bond lengths are similar within the standard uncertainties. The BCPs in these bonds are found at a similar distance from the H atoms (0.25 \AA) and exhibit similar amounts of electron density (2.12 and 2.14 $e \text{ \AA}^{-3}$ for N2–H2 and N3–H3a, respectively). Finally, BCPs of hydrogen bonds are positioned at almost identical distances from the oxygen acceptors (1.30 \AA). The main difference regarding the positions of the BCPs of the two complementary hydrogen bonds arises in the H...BCP, distances which differ by about 0.075 \AA . A comparison of the H...O–N4 angles for these two bonds shows that, in the case of the shorter H3a...BCP distance (N3–H3a...O2 bond), this angle is 120.3°, which is very close to the position of the free electron pair in sp^2 hybridized oxygen. In the second bond, the corresponding H2...O1–N4 angle is quite smaller, 112.6°. One of the reasons could be an additional engagement of the O1 atom in the other relatively strong N3–H3b...O1 hydrogen bonds that connect the formed ribbons to the two-dimensional structures. In contrast to O1, the further engagement of the O2 atom in hydrogen-bonding implies much weaker N1–H1b...O2 interaction. Generally, each of the oxygen atoms is involved in three hydrogen bonds of various strengths. Considering that most of the hydrogen atoms are involved in more than one hydrogen bond, there is a rather continuous dependence of $d(\text{N}\cdots\text{H})$ versus $G(r_{\text{ep}})$ as suggested by Espinosa et al.³⁹

Net Atomic Charges. Net atomic charges derived from κ -model^{13a} and integration over the atomic basins²² are given in Table 5. The different partitioning methods cause the differences between the obtained values; however, the general trend is roughly the same. The nitrogen atoms of the TSC ligand are all negatively charged, with the lowest value found for the terminal thioamide N3 atom. The thioamide C1 atom, which is placed between the two electronegative nitrogen and sulfur

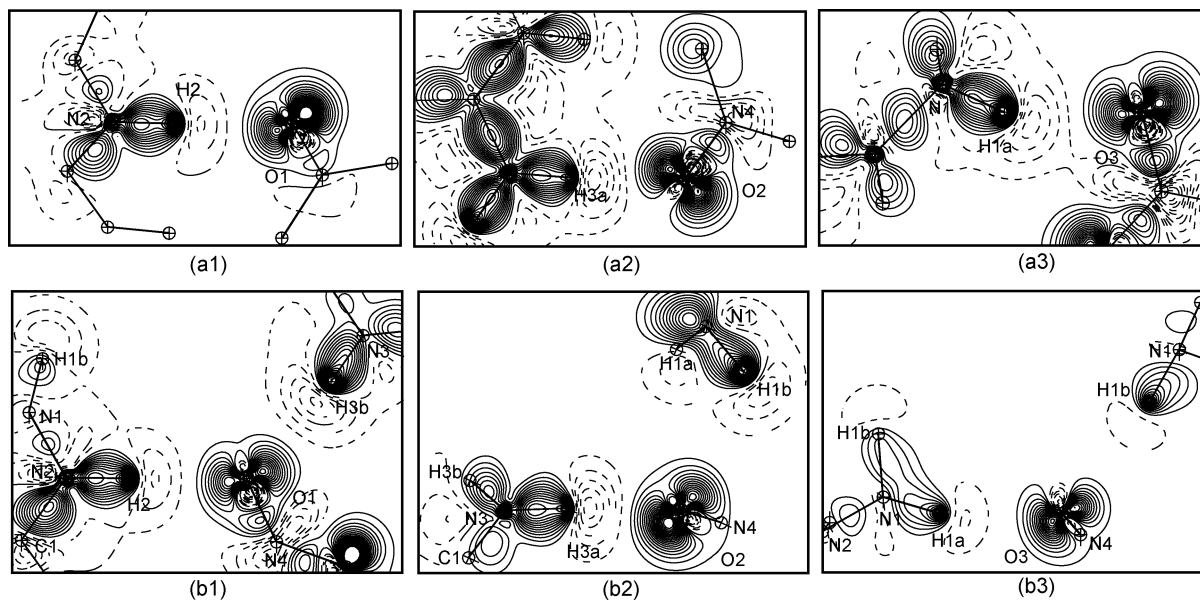


Figure 7. Hydrogen bond static electron deformation density maps. (a) The maps are plotted in the plane containing the strongest hydrogen bond connected, respectively, to O1, O2, and O3. (b) The maps are plotted in the plane defined by the oxygen atom and the pair of hydrogen atoms that forms the two strongest hydrogen bonds. The contour interval is $0.05 \text{ e } \text{\AA}^{-3}$.

TABLE 5: Net Atomic Charges

atom	κ	AIM
Zn1	1.45(4)	0.61
S1	0.01(5)	0.12
N1	-0.70(8)	-0.73
N2	-0.24(7)	-0.83
N3	-0.99(9)	-1.22
N4	0.62(5)	0.65
C1	0.15(8)	0.73
O1	-0.59(4)	-0.54
O2	-0.45(4)	-0.56
O3	-0.53(4)	-0.57
H1a	0.38(5)	0.53
H1b	0.37(5)	0.45
H2	0.28(5)	0.50
H3a	0.45(6)	0.59
H3b	0.53(5)	0.58

atoms is positively charged. The hydrogen atoms provide the rest of the positive charge of the chelate ligand. Among the hydrogen atoms, those attached to the thioamide N3 are the most positively charged. Both analyses also show that the S atom is the least charged atom in the structure. The charges of the nitrate anion obtained by two different methods are real, $q(\text{NO}_3)_\kappa = -0.95(10) \text{ e}$ and $q(\text{NO}_3)_{\text{AIM}} = -1.02 \text{ e}$.

A more significant difference between two groups of charges emerges if we compare the relative distribution of the positive charge between the Zn atom and the TSC ligands. Namely, the κ -model yielded a high value of charge for the Zn atom equal to $+1.45(4) \text{ e}$. In this case, the Zn atom represents the center of the positive charge, because the each TSC ligand is carrying a much less positive charge of $+0.24(20)$. According to the AIM method, the positive charge is more dissipated within the cation, which resulted in a relatively low positive charge for the Zn atom of $+0.61 \text{ e}$, while the charge of the TSC ligand is higher and equal to $+0.72 \text{ e}$. Such a low integrated charge for the Zn basin could be a consequence of the specific Zn–ligand interaction, which in contrast to the other metal ions does not involve the d orbital. Namely, in the case of the title compound the Zn atom has fully occupied d orbitals, and thus only 4s is introduced in the metal–ligand interaction. Because the 4s orbital is very diffuse in the direct space, it is possible that the charge of Zn is spread out over the ligand, i.e., not localized as

a nonzero 3d electron occupation usually is. Consequently, the net charge integrated over the Zn basin is low.

To verify this explanation, the AIM charges of the $[\text{Zn}(\text{aspirinate})_2(\text{H}_2\text{O})_2]$ compound¹⁷ have been determined. The trends above-described observed in $[\text{Zn}(\text{TSC})_2](\text{NO}_3)_2$ remain in the second complex $[\text{Zn}(\text{aspirinate})_2(\text{H}_2\text{O})_2]$ ($q(\text{Zn})_\kappa = +1.29(4) \text{ e}$ and $q(\text{Zn})_{\text{AIM}} = +1.00 \text{ e}$). The net atomic charges obtained by a κ -refinement, when the tetrahedral Zn is modeled as d¹⁰, are closer than the net charge obtained for the third octahedral complex $[\text{Zn}(\text{C}_4\text{O}_4)(\text{H}_2\text{O})_4]$ when the d orbitals are refined ($+1.97 \text{ e}$).¹⁶

Electrostatic Potential. In addition to the analysis of the electron density distribution, we also derived the electrostatic potential (EP) of $[\text{Zn}(\text{TSC})_2](\text{NO}_3)_2$ in an attempt to obtain a better understanding of its further chemical reactivity. In this analysis, we focused only on the EP generated on the surface on the complex cation. We employed the MOLEKEL graphic tool⁴⁰ to distinguish between the fine differences in positive EP. Thus, Figure 8a displays three-dimensional isodensity surface ($0.007 \text{ e } \text{\AA}^{-3}$) of the complex cation colored in accordance with the EP determined on the basis of data obtained after the multipole refinement. Beside the EP of the complex cation isolated from the crystalline environment, we also present the features of the EP of the isolated gas-phase cation obtained by the quantum mechanical calculation (Figure 8b).

The less positive EP coincides with the conjugated thioamide fragment (Figure 8a). One of the two least positive EP regions is found in the surroundings of S atom (A). The part of the cation surface close to Zn exhibits the middle value of the overall positive EP (B). The second EP minimum (the least positive value) on the complex surface is found in the vicinity of the terminal nitrogen N3, which is also reported as the most negative atom in this structure (C). Starting from this region with the least positive EP, the positive EP increases through the number of successive narrow regions of EP magnitudes (D), finally reaching the highest positive value in the vicinity of the hydrogen atoms attached to the N1 donor (E). The positive contribution of the central metal ion to the EP also appears on the surface of the complex cation (F).

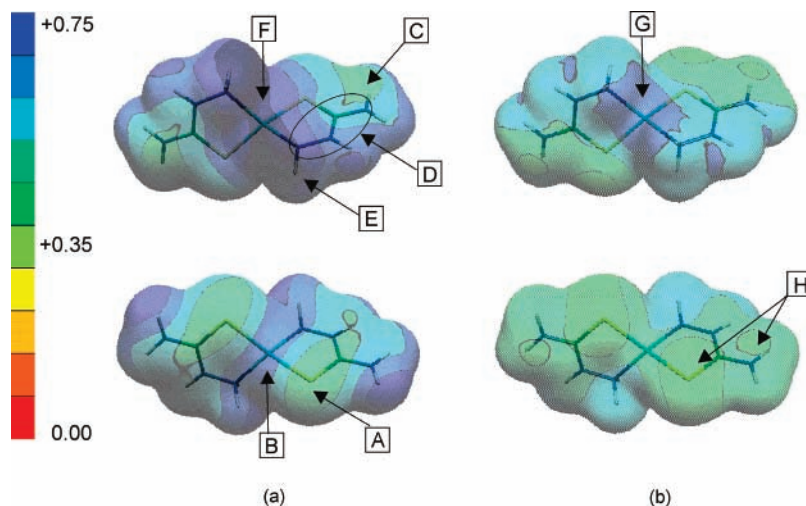


Figure 8. EP ($e \text{ \AA}^{-1}$) generated on the cationic three-dimensional isodensity surface ($0.007 e \text{ \AA}^{-3}$): (a) experimental; (b) theoretical (DFT).

As previously mentioned, the $[\text{Zn}(\text{TSC})_2](\text{NO}_3)_2$ complex, together with some dicarboxylic salts, has been used as the reactant in the synthesis of several supramolecular structures.^{9a,g,d} In each of these structures, the Zn atom within a corresponding cationic TSC building block increases its coordination number to 5 or 6, in contrast to a nickel building block, $[\text{Ni}(\text{TSC})_2]^{2+}$, which often preserves its original coordination number of 4.^{9b,h,10a} The rather nucleophilic zone (F) could be responsible for the increase of the coordination number of Zn in the synthesis of the complexes entering the mentioned supramolecular structures.

The theoretical EP agrees rather well with the described experimentally derived properties for the $[\text{Zn}(\text{TSC})_2]^{2+}$ cation (Figure 8b). The complex cation in the gas phase still retains a nucleophilic zone above the Zn atom (G), suggesting that it is not the result of the influence of the surrounding anions in crystal packing. The least positive EP is again found in the region of the S and N3 atoms (H). Due to the absence of the influence of the crystalline environment, the EP minima are more symmetrically distributed. These trends remain in the two cations $[\text{Zn}(\text{TSC})_2(\text{H}_2\text{O})_2](\text{tere})^{9g}$ and $[\text{Zn}(\text{TSC})_2(\text{H}_2\text{O})_2](\text{fum})^{9d}$ for which the theoretical EP has been computed based on the room-temperature crystal structure geometry, while they are less expressed. The presence of the water molecules, leading to an O_h symmetry for the Zn atom, does not significantly influence the EP value near the TSC ligand.

To investigate the coordination abilities of the TSC ligand alone, we have further used the quantum-chemical calculation²⁹ to explore the distribution of the EP within two different forms of this molecule. The trans form of the TSC molecule³⁰ is present in the solid state and thus corresponds to the molecule that enters the complex synthesis. In this uncoordinated form, the atoms S1 and N1 are placed on opposite sides regarding the C1–N2 bond. According to the EP distribution represented in Figure 9a, we can assume that in the trans configuration of the TSC the sulfur atom surrounded by the most negative EP represents the only relevant center of the nucleophile attack and thus the coordination to the central metal ion. The monodentate coordination of the TSC is rare, but in some complexes of Ag the coordination is realized via the S atom.⁴¹ To achieve more stable bidentate coordination, which is also favored by the chelate effect, the only available atom is N1 as it has the free electron pair. The engagement of N1 is also geometrically favorable due to the formation of the very stable five-membered chelate ring. The NS bidentate coordination and the formation of the five-membered chelate is a basic property of almost all

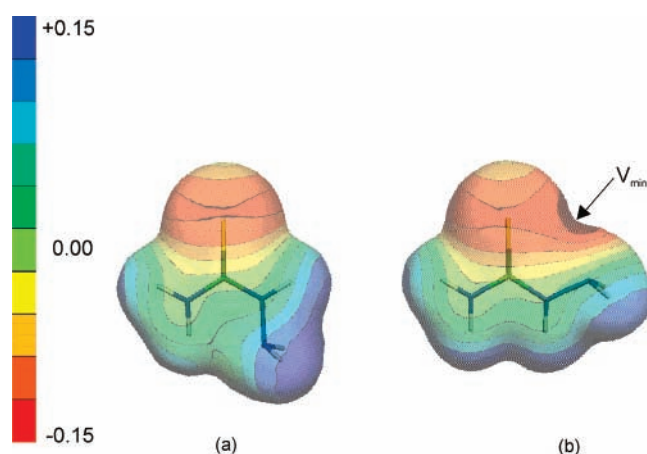


Figure 9. Theoretically determined EP ($e \text{ \AA}^{-1}$) generated on the three-dimensional isodensity surface ($0.007 e \text{ \AA}^{-3}$) of the TSC ligand in the (a) trans and (b) cis configurations.

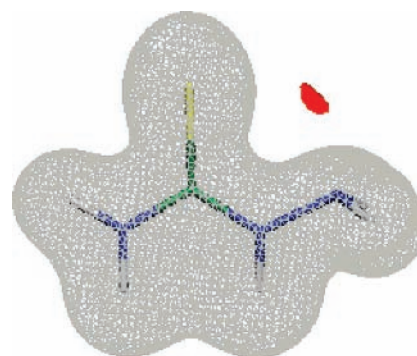


Figure 10. Three-dimensional isopotential surfaces of the coordinated form (cis) of the TSC ligand. Gray and red correspond to $V_{\text{max}} = +0.18 e \text{ \AA}^{-1}$ and $V_{\text{min}} = -0.18 e \text{ \AA}^{-1}$, respectively.

TSC-based compounds.⁵ The distribution of the EP within the cis form of the TSC ligand present in the complexes is given in Figure 9b. It is obvious that in comparison to the trans configuration (Figure 9a) the minimum of the EP is shifted from the S atom toward the place where the binding of central metal ion is expected. This minimum is much deeper than that existing on the S atom in the trans form due to the contribution of the free electron pair of the N1 atom. Figure 10 represent the isopotential surface of the coordinated form of TSC, which confirms that the EP minimum is located exactly between the donor atoms in the place of metal coordination. It is worth

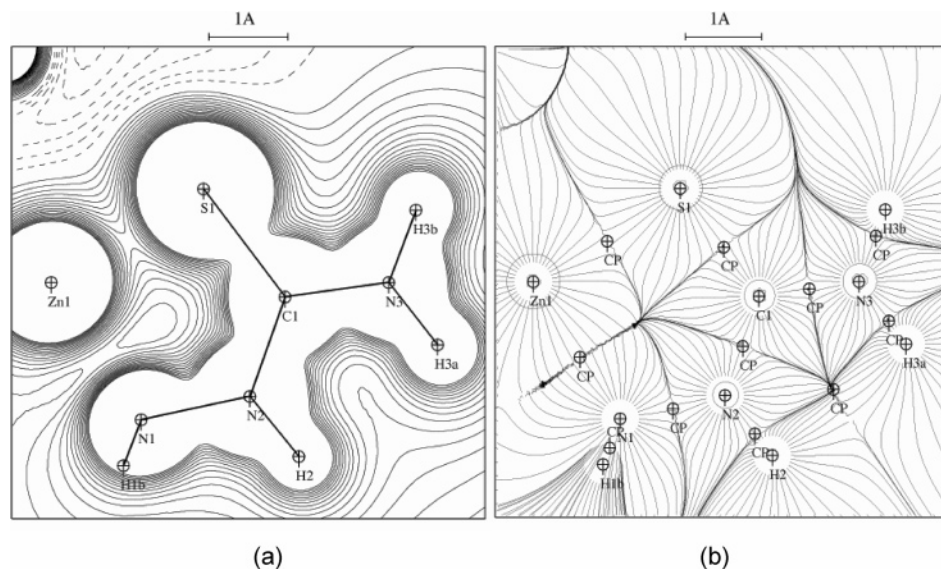


Figure 11. (a) EP in the Zn–TSC ligand plane. Contour intervals are $0.05 \text{ e } \text{\AA}^{-1}$, negative contours are dashed, and zero contour is omitted. (b) Electric field lines in the same plane. Critical points are indicated as “CP”.

mentioning that the cis configuration of TSC present in the complexes also causes the redistribution of the positive EP generated by its hydrogen atoms. The positive EP of the ligand is joined into a broad region (Figure 9b) that in formed bis-(TSC) compounds (takes the lateral sides and) symmetrically surrounds the complex unit. In the presence of the appropriate hydrogen-bonding acceptor, this unit becomes defined building block, as is the case with the above-mentioned supramolecular structures.

Topology of the Electrostatic Potential. The electrostatic potential $\Phi(\mathbf{r})$ (hereafter EP) is one of the derived properties that is directly related to the reactivity of molecules.^{13a,42} Electrophilic and nucleophilic regions are easily revealed and can serve in the quantitative electrostatic characterization of the chemical system and in the chemical activity prediction as well. Topographical characteristics of the EP are complementary to those of the electron density. The gradient $\mathbf{E}(\mathbf{r}) = -\nabla\Phi(\mathbf{r})$ of EP, that is, the electric field, can be calculated analytically from the Hansen–Coppens model used in the experimental electron density refinement.³³ On the basis of this model, two of the authors have developed the FIELD program for the calculation and visualization of the electric field lines around the molecules.⁴³ As for the electron density, the molecular space is partitioned into pseudo-atomic basins or volumes delimited by the zero flux surfaces of the electric field. These correspond to electro-neutral space units in which the electron density concentrates to screen the positive contribution of the nuclear charges to the EP. Contrary to the electron density $\rho(\mathbf{r})$, which is a local property and positive everywhere around the chemical system, EP can be a sharp function that changes its sign in particular regions where the electronic concentration dominates. This gives rise to open basins for positive atoms such as peripheral hydrogens and closed and smallest ones for electronegative atoms such as O and N. We emphasize here that these basins correspond to neutral charges, while those of electron density gradients define the atomic volume in the molecule and therefore its charge transfer. The electric field and electron density gradient offer complementary physical methods to separate the intramolecular space between atoms, and therefore the corresponding atomic basins overlap. The topology of EP also displays critical points (CPs) positioned by a vector \mathbf{r}_{cp} in the unit cell) similar to those of the electron density, (3, -1) saddle, (3, -3) local maximum, (3, +3) local

minimum, but also ring (3, +1) CPs and so on. Three is here the number of nonzero eigenvalues λ_1, λ_2 , and λ_3 of the Hessian matrix of $\Phi(\mathbf{r})$, and the second numbers -3, -1, +1, and +3 are the sums of the algebraic signs of λ_i . The eigenvector associated with λ_3 is conventionally chosen along the atomic link. Poisson’s equation $\nabla^2\Phi(\mathbf{r}) = -4\pi\rho(\mathbf{r})$ is valid everywhere inside or outside the chemical system and relates the two properties. Saddle (3, -1) CPs are generally found between a pair of covalently bonding atoms or in hydrogen bonds. At these positions, the electric field and thus the electric force on a probe charge vanishes, showing the balance between the two screened nuclear charges. As also remembered by Tsirelson et al.,⁴⁴ the electrostatic energy density proportional to the square of the electric field modulus reaches zero at all CPs.

Figure 11a displays the EP calculated in the plane containing the Zn cation and the TSC ligand. As can be expected for a cationic entity, the EP is positive in the vicinity of the metal–ligand complex. In the top-left of Figure 11a, the negative region (with a minimum of $-0.3 \text{ e } \text{\AA}^{-1}$) is due to the proximity of the NO_3^- anion. In the same plane, Figure 11b depicts the electric field lines generated by the Zn–TSC complex. In the plane of this figure, all CPs are of the (3, -1) type, except two (3, +1) ring CPs found between H2 and H3a (folding-induced CP) and that corresponding to the Zn1–S1–C1–N2–N1 ring here under the considered plane. As previously mentioned, the gradient vector lines define closed and open atomic basins with different shapes, structures, and sizes. Internal atoms such as C1, N2, and N3 display triangularly shaped closed basins, whereas peripheral H2, H3a, and H3b have extended basins. It is worthy to note that the S1 sulfur atom has the largest basin even when compared to that of the metal. This is in agreement with the almost neutral net charge reported in the previous section for S1, which behaves as an isolated atom with a dominating nuclear charge contribution to the EP. Another interesting plane is that containing the double hydrogen bond occurring between the TSC ligand and the NO_3^- anion. EP features are shown in Figure 12–a, and the electric field lines are shown in Figure 12b. In addition to the inner (3, -1) CPs of the TSC ligand, those characterizing the N2–H2 \cdots O1 and N3–H3a \cdots O2 hydrogen bonds now appear in Figure 12b.

Table 6 gives the topographical features of the EP generated around the Zn–TSC complex. As pointed out in a prior electric field study,⁴³ the CP atomic distances define the van der Waals

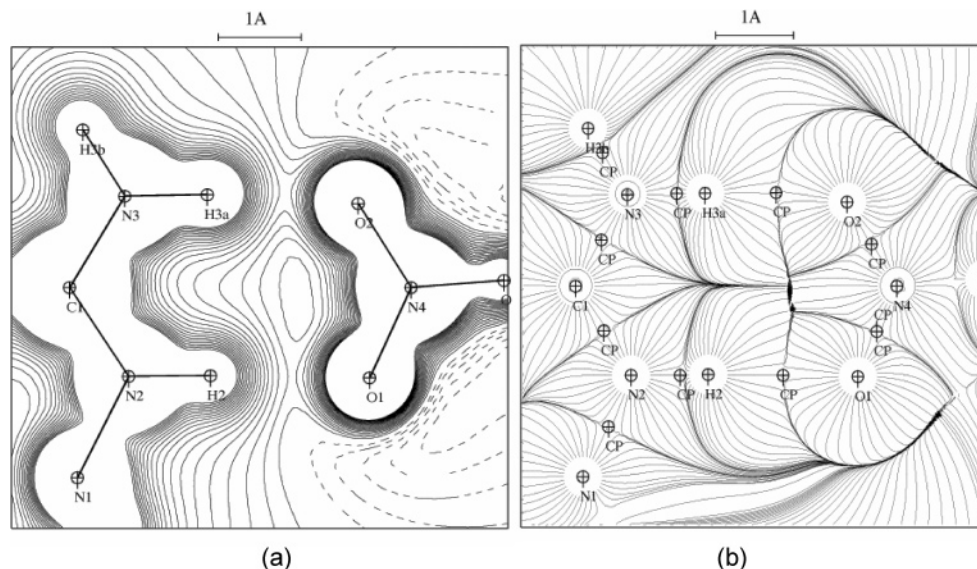


Figure 12. (a) EP in the TSC–NO₃ double hydrogen bonds plane. Contour intervals are 0.05 e Å⁻¹, negative contours are dashed, and zero contour is omitted. (b) Electric field lines in the same plane. Critical points are indicated as “CP”.

TABLE 6: Topological Properties of the Electrostatic Potential for the Covalent Bonds and the Hydrogen Bonds^a

bond	d_1	d_2	$\rho(r_{cp})$	λ_1	λ_2	λ_3	$\Phi(r_{cp})$
Zn1–N1	1.155	0.945	0.632	-0.062	-0.029	0.723	0.225
Zn1–S1	1.102	1.174	0.404	-0.129	-0.117	0.650	0.463
N1–N2	0.707	0.706	2.128	-0.911	-0.867	3.905	1.670
C1–N2	0.674	0.668	2.535	-1.124	-0.991	4.650	1.874
C1–N3	0.668	0.659	2.622	-1.183	-1.029	4.834	1.900
C1–S1	0.776	0.944	1.459	-0.505	-0.439	2.403	1.204
O1–N4	0.624	0.632	3.119	-1.610	-1.587	6.317	1.974
O2–N4	0.625	0.631	3.141	-1.608	-1.575	6.324	2.000
O3–N4	0.617	0.625	3.186	-1.719	-1.681	6.586	2.003
N1–H1a	0.632	0.365	2.340	-2.038	-1.936	6.314	2.104
N1–H1b	0.653	0.377	2.198	-1.775	-1.689	5.662	1.869
N2–H2	0.629	0.361	2.329	-2.141	-2.004	6.474	2.169
N3–H3a	0.635	0.371	2.366	-1.951	-1.845	6.162	1.991
N3–H3b	0.625	0.359	2.438	-2.147	-2.039	6.624	2.085
hydrogen bonds	d_1	d_2	$\rho(r_{cp})$	λ_1	λ_2	λ_3	$\Phi(r_{cp})$
N3–H3a···O2	0.921	0.930	0.347	-0.128	-0.102	0.577	0.245
N2–H2···O1	0.963	0.962	0.308	-0.092	-0.070	0.471	0.131
N1–H1a···O3	1.040	0.960	0.304	-0.080	-0.060	0.444	0.085
N3–H3b···O1	1.118	0.975	0.269	-0.081	-0.061	0.411	-0.044
N1–H1b···O3	1.266	1.032	0.209	-0.044	-0.027	0.279	-0.175

^a $\Phi(r_{cp})$ represents the electrostatic potential (in e Å⁻¹). The other properties and units are defined in the footnote to Table 3.

radii. Except for the N1–N2 bond, all others are heteroatomic links. That means that the contributions of the nuclear charges to the EP are in principle dissymmetrical. That holds particularly true for N–H bonds where the CP is pushed toward the H atoms ($\langle d_1 \rangle = 0.63$ Å and $\langle d_2 \rangle = 0.36$ Å) and for C1–S1 ($d_1 = 0.78$ Å and $d_2 = 0.94$ Å). However, for all other bonds, even for Zn–N and Zn–S, CPs are located approximately at the midpoint of the atomic link. It is worth noting that each atom shows directionally van der Waals radii referring to the type of bonds and atoms involved. In Table 6 are also reported the values of $\rho(r_{cp})$ and $\Phi(r_{cp})$ for each bond. For all covalent bonds, these values are greater than unity, reflecting here the electron accumulation and the positive high value of potential at the vicinity of the nuclei. It is an expected result because only the diffuse 4s orbital of the metal is involved in the interaction with the ligand and the 3d shell was found unperturbed. In the last

part of Table 6, the hydrogen bond characteristics of the title complex are given. The accumulation of electron density at the CPs is in the range of 0.2–0.3 e Å⁻³. However, we can note that for the two last longer bonds ($H\cdots O \geq 2$ Å), $\Phi(r_{cp})$ becomes negative. The eigenvalues of the Hessian matrix of EP ($-1/4\pi$ is included to compare directly to ρ) shows positive values for λ_3 in the bond direction and negative values in the perpendicular ones. According to Poisson’s equation, that is, $\rho(r_{cp}) = \lambda_1 + \lambda_2 + \lambda_3$, these values reflect the electron density accumulation (λ_i positive)/depletion (λ_i negative) at the EP critical points. As expected, λ_3 is higher than λ_1 or λ_2 , which corresponds to the axial symmetry of electron density when $\lambda_1 = \lambda_2$.

According to the Hellmann–Feynman theorem,⁴⁵ the electric field at the nuclear positions is zero ((3, -3) CPs), but EP does not vanish. The values of EP at these particular points are in relation to the core–electron binding energy.⁴⁴ This is particularly interesting for the hydrogen atom with its single electron. Accordingly, Galebov et al.⁴⁶ emphasized the usefulness of the electrostatic potential in nuclear sites (EPNs, corresponding to (3, -3) CPs defined above) as hydrogen-bonding reactivity parameters. The authors found an excellent correlation between the theoretically determined values of EPN at the site of the hydrogen atom and the energies of hydrogen bond formation. Considering the significant hydrogen donating capacity of [Zn(TSC)₂]²⁺, we decided to employ this quantity in further analysis of its hydrogen-bonding features. We derived the EPN values³³ for [Zn(TSC)₂](NO₃)₂ extracted from the crystalline environment on the basis of the experimental data obtained after the multipole refinement (Table 7, 1). In addition, we determined the values of EPN for isolated gas-phase [Zn(TSC)₂](NO₃)₂ (2) and its cation [Zn(TSC)₂]⁺² (3) from quantum-chemical calculations. The theoretical EPN values were also derived for two octahedral cations [Zn(TSC)₂(H₂O)₂]²⁺, which are real building blocks of the supramolecular structures [Zn(TSC)₂(H₂O)₂](tere) (4)^{9g} and [Zn(TSC)₂(H₂O)₂](fum) (5).^{9d} Each of these structures exhibits the same feature; namely, each of them forms the strongest, complementary hydrogen bonds with the same N2–H2, N3–H3a donor set. Finally, the EPN values were also calculated for different configurations of the neutral TSC ligand (6 and 7)

TABLE 7: EPN Values (in a.u.) in the Title Compound (1–3), in Similar Supramolecular Building Blocks (4 and 5), and for Different Forms of the TSC Ligand (6–8)^a

label	1	2	3	4	5	6	7	8
compound	$[\text{Zn}(\text{TSC})_2](\text{NO}_3)_2$	$[\text{Zn}(\text{TSC})_2](\text{NO}_3)_2$	$[\text{Zn}(\text{TSC})_2]^{2+}$	$[\text{Zn}(\text{TSC})_2(\text{H}_2\text{O})_2]^{2+}$	$[\text{Zn}(\text{TSC})_2(\text{H}_2\text{O})_2]^{2+}$	TSC	TSC	TSC ⁺
geometry	this work	this work	this work	ref 9g	ref 9d	ref 30	this work	ref 31
metal	T_d	T_d	T_d	O_h	O_h			
configuration	<i>cis</i>	<i>cis</i>	<i>cis</i>	<i>cis</i>	<i>cis</i>	<i>trans</i>	<i>cis</i>	<i>cis</i>
state	crystal	gas phase	gas phase	gas phase	gas phase	gas phase	gas phase	gas phase
Zn	-142.5002	-141.7899	-141.5911	-141.6274	-141.6429			
S1	-59.4860	-59.1346	-58.9355	-58.967	-58.9724	-59.2697	-59.2722	-59.0784
N1	-18.4693	-18.1899	-17.9859	-18.023	-18.0239	-18.3034	-18.3229	-17.9813
N2	-18.3939	-18.2207	-17.9931	-18.021	-18.0193	-18.2961	-18.2897	-18.0732
N3	-18.4669	-18.2721	-18.0481	-18.070	-18.0685	-18.3300	-18.3248	-18.1502
N4	-18.4967	-18.1395						
C1	-14.7964	-14.5362	-14.3256	-14.353	-14.3522	-14.6331	-14.6301	-14.4448
O1	-22.6694	-22.3511						
O2	-22.6259	-22.3559						
O3	-22.6789	-22.3677						
H1a	-0.9140	-0.9093	-0.7060	-0.7345	-0.7286	-1.0137	-1.0316	-0.7193
H1b	-1.0089	-0.9092	-0.7066	-0.7375	-0.7378	-1.0123	-1.0320	-0.7314
H2	-0.8925	-0.9389	-0.6999	-0.7247	-0.7208	-1.0008	-0.9944	-0.7715
H3a	-0.8792	-0.9601	-0.7264	-0.7440	-0.7456	-1.0060	-0.9954	-0.8161
H3b	-0.9066	-0.9457	-0.7345	-0.7547	-0.7518	-1.0070	-1.0029	-0.8257
extra H								-0.7282
Ow				-22.0468	-22.0269			
H1w				-0.7291	-0.7047			
H2w				-0.7264	-0.7047			

^a The values are determined by POTNUC³³ for case **1** and by Gaussian²⁹ for cases **2–8**. In bold are the least negative EPNs for hydrogen.

and for its protonated form TSCH⁺ (**8**) from the corresponding chloride salt.³¹

The EPN values derived for all of the complex cations in the gas phase (**3–5**) (including the one for the title compound) follow an identical pattern. The least negative EPN value (in bold in Table 7) is found for the H2 atom attached to hydrazine N2, then follow H1a and H1b attached to coordinated hydrazine N1, and finally H3a and H3b from the thioamide N3. This should be an indication of the hydrogen's reactivity toward hydrogen bond formation (pattern and sequence) and an indication of the relative strength of the formed hydrogen bonds and therefore their corresponding bond energies. According to these results, in each of these cations, the H2 atom shows the highest affinity for hydrogen bonding. This atom is the one that is involved in complementary hydrogen bonding; however, its pair H3a has a more negative EPN value, meaning that its tendency to form the hydrogen bonds is slightly less than that for hydrogens attached to N1. Despite these arguments, in the above-mentioned crystal packings of $[\text{Zn}(\text{TSC})_2](\text{NO}_3)_2$, $[\text{Zn}(\text{TSC})_2(\text{H}_2\text{O})_2](\text{tere})$,^{9g} and $[\text{Zn}(\text{TSC})_2(\text{H}_2\text{O})_2](\text{fum})$,^{9d} the H3a atom is always part of the donor set for complementary hydrogen bonding. It seems that suitable, almost parallel orientation of the H2, H3a donor set toward the corresponding acceptors (torsion H2–N2–N3–H3a = 6.9°) makes the engagement of the H3a atom in complementary hydrogen bonds more favorable than for the atoms H1a and H1b (torsion H2–N2–N3–H1 = 50.9° and -66.2°, respectively).

In the case of the whole $[\text{Zn}(\text{TSC})_2](\text{NO}_3)_2$ molecule in the gas phase (Table 7, **2**), the EPN values become more negative. These values are particularly decreasing for the H2, H3a atoms, which form the hydrogen bonds to the present anion. The experimental EPNs (Table 7, **1**) cannot be directly compared to theoretical EPNs because they are generally lower than the gas-phase values. It is interesting to note that, in contrast to the gas-phase cases, the EP at the hydrogen sites of the molecule from the crystal lattice reflects the present state of the hydrogen bonding regarding their strengths. The highest EPN values are found for the H2 and H3a donor set, then follow H3b and H1a, which are involved in hydrogen bonds of similar strengths, and finally H1b, which is engaged in the least strong N1–H1b...O3 hydrogen bond.

The EPN values of the two neutral TSC forms (Table 7, **6** and **7**) are mutually similar and suggest the lower tendency of the hydrogen atoms to enter the hydrogen bonding. The protonation of the ligand (Table 7, **8**) obviously increases the EPN values of the corresponding hydrogen atoms, particularly those attached to the protonated nitrogen atom. It is interesting to note that the EPN values of the listed complex cations (**3–5**) are similar to those found for the protonated ligand. The positively charged metal ion spread its charge to the coordinated ligands, causing the redistribution of the electron density. This significantly increases the EPN values of the hydrogen atoms and stimulates the engagement of ligand in hydrogen bonds. It can be suggested that by coordination to the metal ion the TSC ligand increases its capacity for hydrogen bonding to the level of the protonated ligand.

Conclusion

From the first experimental charge density study on a thiosemicarbazide-based complex compound and some quantum calculations, we have been able to point out some main results concerning the electrostatic properties of this compound.

(i) According to the results of the electron density distribution and the topological analysis, the TSC ligand represents a highly delocalized system. The resonance effect particularly increases the amount of the negative charge and thus the donor abilities of the S atom. The coordination bond between Zn and S atoms is the result of the polarization of the torus-shaped electron density of the free electron pair of the S atom toward the central metal ion. In contrast to the S atom, the free electron pair of the N atom is clearly directed toward the Zn atom. The corresponding values of ρ at the BCPs are 0.52 and 0.41 e \AA^{-3} for Zn–N1 and Zn–S1 bonds, respectively. Both coordination bonds can be classified as polar covalent.

(ii) The nine hydrogen bonds stabilize the crystal structure of $[\text{Zn}(\text{TSC})_2](\text{NO}_3)_2$. The structure also contains complementary hydrogen bonding, intrinsically characteristic for the majority of TSC-based supramolecular structures. The complementary hydrogen bonds are formed between the pair of donors from the complex cation and the nitrate oxygen atoms as acceptors. The complementary bonds slightly differ in their

topological values. The lower amount of ρ at the BCP is found in the case of the bifurcated N3–H3a•••O1 hydrogen bond. The topological characteristics of the O1–N4 and O2–N4 bonds whose O atoms are involved in complementary hydrogen bonding are similar.

(iii) The EP of the complex part of the molecule that enters the supramolecular structures has been derived. The significantly high positive EP found in the region of the Zn atom suggests that the increase of the coordination number of Zn (by coordination of the additional ligands) in the supramolecular complexes could be induced by this property. The theoretical calculations show that in the gas phase this nucleophilic zone is retained.

(iv) The topologic features of the EP in the vicinity of the Zn atom confirm that the Zn–S or Zn–N bonds are weak bonds. Internal atoms such as C1, N2, and N3 display triangularly shaped closed basins, whereas peripheral H2, H3a, and H3b have extended basins.

(v) The EPN values calculated by the DFT method for several TSC complexes entering supramolecular structures show an identical sequence of hydrogen reactivity toward hydrogen bonding. These values suggest that in each of the complexes the hydrazine fragment N2–H2 shows the highest tendency to form a hydrogen bond; however, the affinity of the other donor from the complementary pair is less pronounced. It can be suggested that the formation of the strongest, complementary hydrogen bonding in the crystal is rather a consequence of the suitable geometrical orientation of the H2 and H3a atoms than their preferable reactivity. The EP at the hydrogen sites of the molecule retrieved from the crystal lattice reflects the present state of the hydrogen bonding regarding their strength.

Acknowledgment. The authors thank Dr. B. Courcot (UMR 8580, currently a postdoc at Prince of Wales Medical Research Institute, Sydney, Australia) for help and constructive discussions concerning the theoretical discussions. This work is as part of a project (codirected by A. Spasojević-de Biré and G. A. Bogdanović) within the Franco–Serbian bilateral program “Pavle Savić 2007”. S.B.N. and G.A.B thank the Ministry of Science of the Republic of Serbia for financial support (Projects Nos. 142010 and 142028).

Supporting Information Available: Crystallographic experimental details, fractional coordinates, atomic thermal parameters, κ , κ' , P_{val} , and P_{lm} , multipole parameters, geometrical parameters, and additional residual and deformation density maps for both strategies used in the multipole refinement. This material is available free of charge via the Internet at <http://pubs.acs.org>.

References and Notes

- (1) Tapiero, H.; Tew, K. D. *Biomed. Pharmacother.* **2003**, *57*, 399.
- (2) Lipscom, W. N.; Strater, N. *Chem. Rev.* **1996**, *96*, 2375.
- (3) Dudev, T.; Lim, C. *J. Am. Chem. Soc.* **2000**, *122*, 11146.
- (4) Clark-Baldwin, K.; Tierney, D. L.; Govindaswamy, N.; Gruff, E. S.; Kim, C.; Berg, J.; Koch, S. A.; Penner-Hahn, J. E. *J. Am. Chem. Soc.* **1998**, *120*, 8401.
- (5) (a) Gómez Quiroga, G.; Navarro Ranninger, C. *Coord. Chem. Rev.* **2004**, *248*, 119. (b) Casas, J. S.; García-Tasende, M. S.; Sordo, J. *Coord. Chem. Rev.* **2000**, *209*, 197. (c) Dittes, U.; Vogel, E.; Keppler, B. K. *Coord. Chem. Rev.* **1997**, *163*, 345. (d) West, D. X.; Liberta, A. E.; Padhye, S. B.; Chikate, R. C.; Sonawane, P. B.; Kumbhar, A. S.; Yerande, R. G. *Coord. Chem. Rev.* **1993**, *123*, 49.
- (6) (a) Beraldo, H. *Quim. Nova* **2004**, *27*, 461. (b) Beraldo, H.; Gambino, D. *Mini-Rev. Med. Chem.* **2004**, *4*, 31.
- (7) Cowley, A. R.; Davis, J.; Dilworth, J. R.; Donnelly, P. S.; Dobson, R.; Nightingale, A.; Peach, J. M.; Shore, B.; Kerr, D.; Seymour, L. *Chem. Commun.* **2005**, 845.
- (8) Kovala-Demertzi, D.; Yadav, P. N.; Wiecek, J.; Skoulika, S.; Varadinova, T.; Demertzis, M. A. *J. Inorg. Biochem.* **2006**, *100*, 1558.
- (9) (a) Burrows, A. D.; Harrington, R. W.; Mahon, M. F.; Teat, S. J. *CrystEngComm* **2005**, *7*, 388. (b) Burrows, A. D.; Harrington, R. W.; Mahon, M. F.; Teat, S. J. *Cryst. Growth Des.* **2004**, *4*, 813. (c) Burrows, A. D.; Harrington, R. W.; Mahon, M. F. *Eur. J. Inorg. Chem.* **2003**, 766. (d) Babb, J. E. V.; Burrows, A. D.; Harrington, R. W.; Mahon, M. F. *Polyhedron* **2003**, *22*, 673. (e) Burrows, A. D.; Harrington, R. W.; Mahon, M. F.; Teat, S. J. *CrystEngComm* **2002**, *22*, 539. (f) Burrows, A. D.; Harrington, R. W.; Mahon, M. F. *CrystEngComm* **2000**, *2*, 77. (g) Burrows, A. D.; Menzer, S.; Mingos, D. M. P.; White, A. J. P.; Williams, D. J. *J. Chem. Soc., Dalton Trans.* **1997**, 4237. (h) Burrows, A. D.; Mingos, D. M. P.; White, A. J. P.; Williams, D. J. *Chem. Commun.* **1996**, 97.
- (10) (a) Li, S.-L.; Usman, A.; Razak, I.-A.; Fun, H.-K.; Wu, J.-Y.; Tian, Y.-P.; Jiang, M.-H.; Chen, Z.-Y. *Acta Crystallogr., Sect. C* **2003**, *59*, m181. (b) Fun, H.-K.; Wu, J.-Y.; Tian, Y.-P.; Jiang, M.-H.; Chen, Z.-Y. *Acta Crystallogr., Sect. E* **2003**, *59*, 199. (c) Novaković, S. B.; Bogdanović, G. A.; Leovac, V. M. *Inorg. Chem. Commun.* **2005**, 8, 9.
- (11) (a) Etter, M. C. *Acc. Chem. Res.* **1990**, *23*, 120. (b) Etter, M. C. *J. Phys. Chem.* **1991**, *95*, 4601.
- (12) Sun, D.; Cao, R.; Liang, Y.; Shi, Q.; Hong, M. *J. Chem. Soc., Dalton Trans.* **2001**, 2335.
- (13) (a) Coppens, P. *X-ray Charge Densities and Chemical Bonding*; Oxford University Press: New York, 1997. (b) Coppens, P. *Acta Crystallogr., Sect. A* **1998**, *54*, 779. (c) Koritsanszky, T. S.; Coppens, P. *Chem. Rev.* **2001**, *101*, 1583.
- (14) Cotton, F. A.; Wilkinson, G. W. *Advanced Inorganic Chemistry: A Comprehensive Text*, 2nd ed.; Interscience Publishers: New York, 1966; p 610.
- (15) O'Toole, N. J.; Streltsov, V. A. *Acta Crystallogr., Sect. B* **2001**, *57*, 128.
- (16) Lee, C.-R.; Wang, C.-C.; Chen, K.-C.; Lee, G.-H.; Wang, Y. *J. Phys. Chem. A* **1999**, *103*, 156.
- (17) Spasojević-de Biré, A.; Bouhaida, N.; Kremenović, A.; Morgant, G.; Ghermani, N.-E. *J. Phys. Chem. A* **2002**, *106*, 12170.
- (18) (a) Romanenko, G. V.; Saveleva, Z. A.; Larionov, S. V. *Zh. Strukt. Khim.* **1999**, *40*, 593. (b) Tong, Y.-X.; Su, C.-Y.; Zhang, Z.-F.; Kang, B.-S.; Yu, X.-L.; Chen, X.-M. *Acta Crystallogr., Sect. C* **2000**, *56*, 44.
- (19) Allen, F. H. *Acta Crystallogr., Sect. B* **2002**, *58*, 380.
- (20) Row, T. N. G.; Desiraju, R. G. *Acta Crystallogr., Sect. B* **2006**, *62*, 118.
- (21) Novakovic, S. B.; Fraisse, B.; Bogdanovic, G. A.; Spasojevic-de Bire, A. *Cryst. Growth Des.* **2007**, *7*, 191.
- (22) Bader, R. F. W. *Atoms in Molecules: A Quantum Theory*; Clarendon Press: Oxford, U. K., 1990.
- (23) SMART (5.625), SAINT (6.02), and SADABS (2.03): Data Collection and Processing Software for the SMART System; Siemens (BRUKER-AXS) Analytical X-ray Instruments: Madison, WI, 2001.
- (24) Blessing, R. H. *J. Appl. Crystallogr.* **1997**, *30*, 421.
- (25) Hansen, N. K.; Coppens, P. MOLLY Program. *Acta Crystallogr., Sect. A* **1978**, *34*, 909.
- (26) Farrugia, L. J. WINGX Program Package for Structure Solution. *J. Appl. Crystallogr.* **1999**, *32*, 837.
- (27) Kuhs, W. F. *Acta Crystallogr., Sect. A* **1983**, *39*, 148.
- (28) Allen, F. H.; Kennard, O.; Watson, D. G. *J. Chem. Soc., Perkin Trans.* **1997**, S1.
- (29) Frisch, M. J.; Trucks, G. W.; Schlegel, H. B.; Scuseria, G. E.; Robb, M. A.; Cheeseman, J. R.; Montgomery, J. A., Jr.; Vreven, T.; Kudin, K. N.; Burant, J. C.; Millam, J. M.; Iyengar, S. S.; Tomasi, J.; Barone, V.; Mennucci, B.; Cossi, M.; Scalmani, G.; Rega, N.; Petersson, G. A.; Nakatsuji, H.; Hada, M.; Ehara, M.; Toyota, K.; Fukuda, R.; Hasegawa, J.; Ishida, M.; Nakajima, T.; Honda, Y.; Kitao, O.; Nakai, H.; Klene, M.; Li, X.; Knox, J. E.; Hratchian, H. P.; Cross, J. B.; Bakken, V.; Adamo, C.; Jaramillo, J.; Gomperts, R.; Stratmann, R. E.; Yazyev, O.; Austin, A. J.; Cammi, R.; Pomelli, C.; Ochterski, J. W.; Ayala, P. Y.; Morokuma, K.; Voth, G. A.; Salvador, P.; Dannenberg, J. J.; Zakrzewski, V. G.; Dapprich, S.; Daniels, A. D.; Strain, M. C.; Farkas, O.; Malick, D. K.; Rabuck, A. D.; Raghavachari, K.; Foresman, J. B.; Ortiz, J. V.; Cui, Q.; Baboul, A. G.; Clifford, S.; Cioslowski, J.; Stefanov, B. B.; Liu, G.; Liashenko, A.; Piskorz, P.; Komaromi, I.; Martin, R. L.; Fox, D. J.; Keith, T.; Al-Laham, M. A.; Peng, C. Y.; Nanayakkara, A.; Challacombe, M.; Gill, P. M. W.; Johnson, B.; Chen, W.; Wong, M. W.; Gonzalez, C.; Pople, J. A. *Gaussian 03*, revision B.04; Gaussian, Inc.: Wallingford, CT, 2004.
- (30) Andreetti, G. D.; Domiano, P.; Gasparri, G. F.; Nardelli, M.; Sgarabotto, P. *Acta Crystallogr., Sect. B* **1970**, *26*, 1005.
- (31) Coghi, L.; Lanfredi, A. M. M.; Tiripicchio, A. *J. Chem. Soc., Perkin Trans. 2* **1976**, 1808.
- (32) Steiner, T. *J. Phys. Chem. A* **1998**, *102*, 7041.
- (33) Ghermani, N. E.; Bouhaida, N.; Lecomte, C. *ELECTROS, STATDENS, FIELD+, POTNUC: Computer Program to Calculate Electrostatic Properties from High-Resolution X-ray Diffraction*;

Internal Report; UMR CNRS 7036, Université Henri Poincaré, Nancy 1, France, UMR CNRS 8612, Université Paris XI, France, and Laboratoire LSM, Université Cadi Ayyad, Morocco, 1992–2007.

(34) Souhassou, M. Atomic Properties from Experimental Electron Densities: Program Newprop-Int. In *Proceedings of the 19th European Crystallographic Meeting*, Nancy, France, Aug 25–31, 2000; Abstract S2–m2-p2, p 195 (also LCM3B Internal Report, Université Henri Poincaré, Nancy 1, France).

(35) Abramov, Y. A. *Acta Crystallogr., Sect. A* **1997**, *53*, 457.

(36) (a) Destro, R.; Soave, R.; Barzaghi, M.; Presti, L. L. *Chem.—Eur. J.* **2005**, *11*, 4621. (b) Munshi, P.; Row, T. N. G. *Acta Crystallogr., Sect. B* **2006**, *62*, 612. (c) Espinosa, E.; Molins, E.; Lecomte, C. *Phys. Rev. B* **1997**, *56*, 1820. (d) Dahaoui, S.; Pichon-Pesme, V.; Howard, J. A. K.; Lecomte, C. *J. Phys. Chem.* **1999**, *103*, 6240. (e) Lee, C.-R.; Tan, L.-Y.; Wang, Y. *J. Phys. Chem. Solids* **2001**, *62*, 1613. (f) Pillet, S.; Souhassou, M.; Pontillon, Y.; Caneschi, A.; Gatteschi, D.; Lecomte, C. *New J. Chem.* **2001**, *25*, 131. (g) Guillot, R.; Muzet, N.; Dahaoui, S.; Lecomte, C.; Jelsch, C. *Acta Crystallogr., Sect. B* **2001**, *57*, 567. (h) Munshi, P.; Guru Row, T. N. *Acta Crystallogr., Sect. B* **2002**, *58*, 1011. (i) Hambley, T. W.; Hibbs, D. E.; Turner, P.; Howard, S. T.; Hursthouse, M. B. *J. Chem. Soc., Perkin Trans. 2* **2002**, 235. (j) Hibbs, D. E.; Austin-Woods, C. J.; Platts, J. A.; Overgaard, J.; Turner, P. *Chem.—Eur. J.* **2003**, *9*, 1075. (k) Lee, C. R.; Tang, T. H.; Chen, L.; Wang, Y. *Chem.—Eur. J.* **2003**, *9*, 3112. (l) Ghermani, N. E.; Spasojević-de Biré, A.; Bouhaida, N.; Ouharzoune, S.; Bouligand, J.; Layre, A.; Gref, R.; Couvreur, P. *Pharm. Res.* **2004**, *21*, 598. (m) Leusser, D.; Henn, J.; Kocher, N.; Stalke, D. *J. Am. Chem. Soc.* **2004**, *126*, 1871. (n) Wagner, A.; Flaig, R.; Dittrich, B.; Schmidt, H.; Koritsanzsky, T.; Luger, P. *Chem.—Eur. J.* **2004**, *10*, 2977. (o) Overgaard, J.; Hibbs, D. E. *Acta Crystallogr., Sect. B* **2004**, *60*, 480. (p) Tsirelson, V. G.; Stash, A. I.; Potemkin, V. A.; Rykounov, A. A.; Shutalev, A. D.; Zhurova, E. A.; Zhurov, V. V.; Pinkerton, A. A.; Gurskaya, G. V.; Zavodnik, V. E. *Acta Crystallogr., Sect. B* **2006**, *62*, 676.

(37) (a) Smith, G. T.; Mallinson, P. R.; Frampton, C. S.; Howard, J. A. K. *J. Chem. Soc., Perkin Trans. 2* **1997**, 1329. (b) Kozisek, J.; Hansen, N. K.; Fuess, H. *Acta Crystallogr., Sect. B* **2002**, *58*, 463. (c) Lee, J. J.; Lee, G. H.; Wang, Y. *Chem.—Eur. J.* **2002**, 1821. (d) Tafipolsky, M.; Scherer, W.; Ofele, K.; Artus, G.; Pedersen, B.; Herrmann, W. A.; McGrady, G. S. *J. Am. Chem. Soc.* **2002**, *124*, 5865. (e) Ritchie, J. P.;

Zhurova, E. A.; Martin, A.; Pinkerton, A. A. *J. Phys. Chem. B* **2003**, *107*, 14576. (f) Zhurova, E. A.; Tsirelson, V. G.; Stash, A. I.; Yakovlev, M. V.; Pinkerton, A. A. *J. Phys. Chem. B* **2004**, *108*, 20173. (g) Zhurova, E. A.; Martin, A.; Pinkerton, A. A. *J. Am. Chem. Soc.* **2002**, *124*, 8741.

(38) (a) Iversen, B. B.; Larsen, F. K.; Figgis, B. N.; Reynolds, P. A. *J. Chem. Soc., Dalton Trans.* **1997**, 2227. (b) Hwang, T.-S.; Wang, Y. *J. Phys. Chem. A* **1998**, *102*, 3726. (c) Kozsek, J.; Hansen, N. K.; Fuess, H. *Acta Crystallogr., Sect. B* **2002**, *58*, 463. (d) Bytheway, I.; Figgis, B. N.; Sobolev, A. N. *J. Chem. Soc., Dalton Trans.* **2001**, 3285. (e) Macchi, P.; Schultz, A. J.; Larsen, F. K.; Iversen, B. B. *J. Phys. Chem. A* **2001**, *105*, 9231. (f) Wang, C.-C.; Tang, T.-H.; Wang, Y. *J. Phys. Chem. A* **2000**, *104*, 9566. (g) Kozisek, J.; Fron, M.; Skubak, P.; Popkov, A.; Breza, M.; Fuess, H.; Paulmann, C. *Acta Crystallogr., Sect. A* **2004**, *60*, 510. (h) Pillet, P.; Souhassou, M.; Mathoniere, C.; Lecomte, C. *J. Am. Chem. Soc.* **2004**, *126*, 1219. (i) Farrugia, L. J.; Frampton, C. S.; Howard, J. A. K.; Mallinson, P. R.; Peacock, R. D.; Smith, G. T.; Stewart, B. *Acta Crystallogr., Sect. B* **2006**, *62*, 236.

(39) Espinosa, E.; Lecomte, C.; Molins, E. *Chem. Phys. Lett.* **1998**, 285, 170.

(40) Portmann, S.; Lüthi, H. P. MOLEKEL: An Interactive Molecular Graphics Tool. *Chimia* **2000**, *54*, 766.

(41) Campbell, M. J. *Coord. Chem. Rev.* **1975**, *15*, 279 and references therein.

(42) *Chemical Applications of Atomic and Molecular Electrostatic Potentials: Reactivity, Structure, Scattering, and Energetics of Organic, Inorganic, and Biological Systems*; Politzer, P., Truhlar, D. G., Eds.; Plenum Press: New York, 1981.

(43) Bouhaida, N.; Dutheil, M.; Ghermani, N. E.; Becker, P. *J. Chem. Phys.* **2002**, *116*, 6196.

(44) Tsirelson, V. G.; Avilov, A. S.; Lepeshov, G. G.; Kulygin, A. K.; Stahn, J.; Pietsch, U.; Spence, J. C. H. *J. Phys. Chem. B* **2001**, *105*, 5068.

(45) (a) Feynman, R. P. *Phys. Rev.* **1939**, *56*, 340. (b) Hellmann, H. *Einführung in die Quantenchemie*; Deuticke: Leipzig, Germany, 1937.

(46) Galabov, B.; Bobadova-Parvanova, P.; Ilieva, S.; Dimitrova, V. *J. Mol. Struct.: THEOCHEM* **2003**, *630*, 101 and references therein. (b) Ferrante, F.; La Manna, G. *J. Phys. Chem. A* **2003**, *107*, 91. (c) Galabov, B.; Cheshmedzhieva; Ilieva, D.; Hadjieva, S. B. *J. Phys. Chem. A* **2004**, *108*, 11457. (d) Galabov, B.; Atanasov, Y.; Ilieva, S.; Schaefer, H. F. *J. Phys. Chem. A* **2005**, *109*, 11470.